Hydrothermal pre-treatment, an efficient tool to improve activated carbon performances

Fatma Mbarki, Taher Selmi, Aida Kesraoui, Mongi Seffen, Philippe Gadonneix, Alain Celzard, Vanessa Fierro

Hydrothermal pre-treatment, an efficient tool to improve activated carbon performances

Fatma Mbarki[a,b], Taher Selmi[a], Aida Kesraoui[a], Mongi Seffen[a], Philippe Gadonneix[c], Alain Celzard[c], Vanessa Fierro[c,*]

[a] Laboratory of Energy and Materials (LabEM), High School of Sciences and Technology of Hammam Sousse, Sousse University, BP 4011, Hammam Sousse, Tunisia

[b] Faculty of Sciences of Monastir, Monastir University, 5019 Monastir, Tunisia

[c] Institut Jean Lamour, UMR Université de Lorraine-CNRS 7198, 27 rue Philippe Séguin, BP 21042, 88051 Epinal Cedex 9, France

[*] Corresponding author:
Vanessa Fierro, Tel: +33372749677, e-mail address: vanessa.fierro@univ-lorraine.fr

Abstract

In this study, the successful preparation of activated carbons from Corn Stigmata, either through direct pyrolysis and activation or through a preliminary additional hydrothermal carbonisation (HTC) step, was reported. It was shown that the latter allowed producing higher carbon yield, higher carbon content and higher BET area (A_{BET}) after 2h of activation with CO_2 than what was observed for activated carbons (ACs) prepared in the same conditions but without HTC. The AC having the most developed porous texture, A_{BET} = 1111 m^2/g, was further investigated by FTIR, SEM and potentiometric titration, and its pH at point of zero charge was determined. Its performances in terms of methylene blue (MB) adsorption were studied and discussed in relation to its textural and chemical characteristics. Due to its very heterogeneous surface, the fractal Brouers–Sotolongo model was the most relevant for describing both kinetic and equilibrium adsorption data. The calculated thermodynamic parameters also showed that MB adsorption was spontaneous on this material. The high MB uptake at room temperature, compared to many other results published in the literature, further confirmed the interest of Corn Stigmata-derived hydrochars as precursors of activated carbons.

Keywords: Corn Stigmata; hydrothermal carbonisation; physical activation; activated carbon; methylene blue; adsorption

1. Introduction

Textile and leather industries generate wastewaters containing significant dye contents. Due to the high toxicity and carcinogenic potential of the latter (Georgin et al., 2016), such effluents need to be treated before discharging to natural watercourses. Dye removal can be carried out by various physical and/or chemical methods such as, amongst others, oxidation, electrocoagulation and flocculation, reverse osmosis, chemical precipitation, ultra-filtration, ion exchange and biological processes (Métivier-Pignon et al., 2003; Olad et al., 2010). Adsorption is also considered as an attractive alternative for dye removal, and activated carbons (ACs), due to their highly developed surface area and easy-tuned surface chemistry, are among the most commonly used materials for that purpose (Danish et al., 2018a). Indeed, they can efficiently remove organic and inorganic pollutants (Acosta et al., 2018; Ghouma et al., 2015; Podder and Majumder, 2016; Selmi et al., 2018a).

ACs can be synthesised through two well-known processes: physical and chemical activation. Moreover, many studies have been published, reporting the production of activated carbon by physical activation of biomass (Altenor et al., 2012; Enaime et al., 2017; Gaspard et al., 2006; Selmi et al., 2018a).

Hydrothermal carbonisation (HTC) involves the treatment of an organic precursor in aqueous solution at moderate self-generated pressure (less than 20 bars) and mild temperature (less than 250°C), which are fundamental for the occurrence of several reactions such as hydrolysis, dehydration, condensation, aromatisation and polymerisation (Sevilla and Fuertes, 2009). An insoluble, black carbonaceous solid called hydrochar, which contains higher carbon content than the original material, is thus obtained. Carbon materials are obtained after applying a subsequent pyrolysis step, for increasing the carbon content and improving the textural properties of the final materials.

HTC is attracting growing attention because it also allows stabilising the macrocellular structure of biomass before pyrolysis, and also because the resultant carbons usually have a higher mesoporosity (Selmi et al., 2018a). The final morphology of those materials pre-treated by HTC indeed shows a mixed structure in which the lignin backbone has been preserved and where cellulose produced microspheres. HTC of biomass is also interesting for producing ACs. Some publications have reported the production of activated carbons using the HTC process before pyrolysis as a route to improve the porosity of these materials, preserving at the same time the spherical morphology of the particles.

For instance, Laginhas et al. (2015) prepared activated carbons from chitosan with a procedure combining different activation methods. The optimal carbonisation conditions were 200ºC for 24h using a water/precursor ratio of 1/6. Tran et al. (2017) have synthesised an activated carbon from golden shower via hydrothermal carbonisation in the presence of acrylic acid, which was used to enhance the density of oxygen groups on the AC surface without significantly affecting the textural properties. Falco et al. (2013) reported that carbon derived from rye straw hydrochar resulted in a BET area up to 2200 m^2/g and in a CO_2 uptake of 20 mmol/g at 25°C and 40 bar. Selmi et al. (2018) used HTC of *Agave Americana* fibres mixed with *Mimosa* tannin to produce ACs with A_{BET} as high as 1200 m^2/g, and with much more functional groups on their surface.

Corn is extensively used for the production of oil, and thus *Corn Stigmata* (CS) is a renewable and relatively abundant agricultural by-product that has been already used as biosorbent for removing dyes such as indigo carmine and methylene blue from water (Mbarki et al., 2018). In the present study, CS was used as potential AC precursor for the first time in an attempt to valorise such renewable, low-cost and highly abundant biomass. HTC pre-treatment effect on the activation process and final AC texture was analysed and compared to

97 materials directly obtained from pyrolysed CS. Finally, the corresponding performances in
98 terms of methylene blue removal from water were investigated.
99
100 ## 2. Materials and methods
101 ### 2.1. Raw materials
102 Corn Stigmata (CS) were collected in the central Tunisian region of Kairouan in July. They
103 were thoroughly washed, dried and ground as detailed elsewhere (Mbarki et al., 2018) to
104 obtain particles in the range of size 2 – 5 mm. The ash content in CS was determined
105 according to the ASTM E1755 standard; briefly, 1.000g of CS was placed in a crucible and
106 introduced into a muffle furnace at 600°C for 3 h in air atmosphere. Then, the crucible was
107 removed and placed in a desiccator for cooling before being weighed. The ash content in dry
108 basis was calculated as the ratio between the final (ashes) and initial (CS) masses in the
109 crucible, both dry. Ash determination was repeated 3 times and the reported value is the
110 average of the three very similar measurements, with an error of less than 2% in the
111 determined value.
112 Methylene blue (MB) was provided by Sigma Aldrich (purity > 85%). MB solutions with
113 the required concentrations were prepared by diluting a 1 g/L (1000 ppm) stock solution in
114 distilled water.
115
116 ### 2.2. Activated carbon synthesis
117 Two series of ACs were obtained from CS by two processes. On the one hand, 1 g of CS
118 fibres was placed in a quartz boat, placed itself in the quartz tube of a horizontal furnace
119 (Carbolite CTF) continuously flushed with nitrogen flowing at 100 mL/min. The furnace was
120 slowly heated at 1°C/min up to 900°C to obtain a carbon material with a well-developed
121 porous texture, and the final temperature was held for 1h. Then, the furnace was allowed to

cool down to room temperature under nitrogen flow. The resultant carbon was labelled CCS, wherein the first "C" means "carbon".

On the other hand, a second carbon material was prepared by submitting CS to HTC before pyrolysis at 900°C. Approximately 4 g of dried CS were introduced in 40 g of distilled water in a 200 mL Teflon-lined autoclave (Anton Paar). The autoclave was then introduced for 6 h in a ventilated oven pre-heated at 180°C. The choice of HTC conditions ensured total HTC conversion (Braghiroli et al., 2014). After HTC and drying at 105°C, the material was labelled HCS, where "H" means "hydrochar". The HCS sample was then submitted to pyrolysis as described above, and the resultant carbon was labelled CHCS.

Physical activation by action of CO_2 at 900°C was then carried out in the same tubular furnace as the one used for pyrolysis. For that purpose, 1 g of carbon sample, either CCS or CHCS, was heated at 5°C/min up to 900°C under nitrogen flowing at 100 mL/min. Once the final temperature was reached, nitrogen was replaced by carbon dioxide at a flow rate of 60 mL/min during 0.5, 1, 2 or 3h. Next, the furnace was allowed to cool under nitrogen, flowing again at 100 mL/min. The resultant ACs were labelled either ACt_CHCS or ACt_CCS, depending on the precursor, where "AC" refers to "activation" and "t" stands for the activation time (h).

The total yield of the process, Y_T (%), comprising HTC or not, was calculated as follows:

$$Y_T = \frac{m_{AC}}{m_{CS}} \times 100 \quad (1)$$

where m_{AC} is the mass of AC (g), and m_{CS} is the mass of initial CS (g).

2.3. Carbon materials characterisation

Elemental compositions in terms of C, H, N and S contents were determined with a Vario El Cube analyser (Elementar). Oxygen content was determined with the same device in a second step, using a specific protocol. Fourier-transform infrared spectroscopy (PerkinElmer Spectrum

147 Two) was performed to analyse the functional groups on the carbon surface. Experiments were
148 carried out based on samples diluted in KBr pellets according to a 1:100 weight ratio of carbon
149 to KBr.

150 The point of zero charge, pH_{PZC}, and the potentiometric titration experiments were
151 performed with an automatic titrator (905 Titrando, Metrohm, monitored by tiamo software
152 V2.2) as described elsewhere (Selmi et al., 2018a). It is assumed that the carbon materials
153 have acidic sites characterised by their acidity constants, K_a, and that the population of sites
154 can be described by a continuous pK_a distribution function, f(pK_a) (Bandosz et al., 1993;
155 Jagiello et al., 1995). The experimental titration data were converted into a proton-binding
156 curve, from which the distribution of acidity constants was obtained by using the numerical
157 SAIEUS procedure (Jagiello, 1994).

158 The textural characterisation was performed by investigating adsorption-desorption of N_2
159 at -196°C and of CO_2 at 0ºC, using Micromeritics ASAP 2020 and ASAP 2420 automatic
160 devices, respectively. Adsorption data were treated by the Microactive software as described
161 elsewhere (Selmi et al., 2018a). In short, we determined the BET area, A_{BET} (m^2/g), the
162 Gurvitch volume, $V_{0.97}$ ($cm^3\ g^{-1}$), and the Dubinin-Raduskevich (DR) volumes (Dubinin,
163 1989) from nitrogen and carbon dioxide adsorption, $V_{DR,N2}$ (cm^3/g) and $V_{DR,CO2}$ (cm^3/g),
164 respectively. The enhanced 2D-NLDFT model (Jagiello et al., 2019) was applied to both the
165 N_2 and CO_2 adsorption isotherms to calculate the pore size distributions (PSDs). The
166 following parameters were also determined: surface area, S_{NLDFT} (m^2/g), micropore volume
167 (pore width, $w < 2$ nm), $V_{mic,\ NLDFT}$ (cm^3/g), total pore volume, $V_{T,\ NLDFT}$ (cm^3/g), and
168 mesopore volume ($2 < w < 50$ nm), $V_{meso,\ NLDFT}$ (cm^3/g), calculated as the difference $V_{T,\ NLDFT}$
169 - $V_{mic,\ NLDFT}$.

170 The surface morphology of the carbons was investigated with a JEOL JSM 5400 scanning
171 electron microscope.

2.4. Methylene blue (MB) adsorption

The study of MB adsorption was carried out with the AC having the most developed porous texture of the series, taking into account the total surface area A_{Tot}, introduced elsewhere (Fierro et al., 2010; Selmi et al., 2018a) and calculated according to:

$$A_{Tot} = A_{BET}(\mathrm{m^2/g}) \times \frac{Y_T(\mathrm{wt.\%})}{100} \quad (2)$$

MB adsorption capacity of the ACs was determined in batch experiments by adding 50 mg of AC in 50 mL of MB solutions of different known concentrations at pH 10. MB concentrations in the solutions before and after adsorption were determined using a UV-Vis spectrophotometer analysis (Camspec M550) at a wavelength λ_{max} = 663 nm. Adsorption thermodynamic parameters were determined by carrying out MB adsorption at three different temperatures: 20, 30 and 40°C.

To calculate the MB adsorption capacity, Q_t (mg/g), and the MB removal, R (%), the following equations were used:

$$Q_t = \frac{(C_i - C_t) \times V}{m} \quad (3)$$

$$\%R = \frac{C_i - C_f}{C_i} \times 100 \quad (4)$$

where C_i, C_f and C_t (mg/L) are the initial concentration, the final concentration, and the concentration at time t, respectively. V (L) is the volume of solution and m (g) is the mass of AC.

2.4.1. Determination of thermodynamic parameters

Thermodynamic parameters such as Gibbs free energy change ($\Delta G°$, J/mol), enthalpy change ($\Delta H°$, J/mol) and entropy change ($\Delta S°$, J/mol/K) were estimated using the following equations:

$$\Delta G° = -RT \ln K_c \quad (5)$$

$$\ln K_c = \frac{\Delta S^\circ}{R} - \frac{\Delta H^\circ}{RT} \quad (6)$$

where K_c is the equilibrium constant calculated as the ratio of amount of adsorbed MB to amount of MB in solution at equilibrium, T (K) is the temperature, and R is the universal gas constant (8.314 J/mol/K).

2.4.2. Determination of kinetic parameters

Three non-linear models (pseudo-first order, pseudo-second order and the fractal model of Brouers– Sotolongo) were used to evaluate the adsorption rates and to interpret the experimental data obtained.

The equation of the pseudo-first order (PFO) (Lagergren, 1898) reads:

$$\frac{dQ}{dt} = k_1(Q_{e1} - Q_t) \quad (7)$$

where Q_{e1} (mg/g) and Q_t (mg/g) are the amounts of dye adsorbed at equilibrium and at time t (min), respectively, and k_1 (min^{-1}) is the rate constant of pseudo-first-order sorption.

The equation of the pseudo-second order (PSO) (Ho and McKay, 1998, 1999) reads :

$$\frac{dQ}{dt} = k_2(Q_{e2} - Q_t)^2 \quad (8)$$

where k_2 (g/(mg min)) is the rate constant of the pseudo-second-order equation.

The fractal model of Brouers– Sotolongo (BSf) (Brouers and Sotolongo-Costa, 2006) reads :

$$Q_t = Q_{e,BS}\left[1 - \left(1 + (n-1)\left(\frac{t}{\tau_c}\right)^{\alpha}\right)^{\frac{-1}{n-1}}\right] \quad (9)$$

In Equation 9, n is the non-integer reaction order and α is a fractional time exponent related to the fractality of the AC surface. Such fractal character is due to physical and chemical heterogeneities of the surface, and α is a measure of the average energy and width of the adsorption energy distribution E_D according to $\alpha \propto \frac{k\,T}{E_D}$. τ_c (min) is the necessary time to

reach equilibrium (Selmi et al., 2018c; Selmi et al., 2018d), and Q_e (mg/g) is the equilibrium adsorption capacity.

2.4.3. Adsorption isotherms at equilibrium

The adsorption data obtained at equilibrium at 25°C were fitted using four isotherm models: Langmuir, Freundlich, Sips and Brouers-Sotolongo.

The equation of Langmuir model (Langmuir, 1918) reads:

$$Q_e = Q_m . \frac{K_L C_e}{1 + K_L C_e} \quad (10)$$

where K_L (L/mg) is the Langmuir equilibrium constant and Q_m (mg/g) is the maximum sorption capacity.

The equation of Freundlich model (Freundlich, 1906) reads:

$$Q_e = K_F . C_e^{1/n} \quad (11)$$

where K_F (mg/g) $(L/mg)^{1/n}$ is the Freundlich constant indicating the adsorption capacity and n (dimensionless) is a parameter indicating the adsorption affinity and capacity of the adsorbate/adsorbent system.

The equation of Sips model (Sips, 1948) reads:

$$Q_e = \frac{Q_m K_S C_e^{1/m}}{1 + K_S C_e^{1/m}} \quad (12)$$

where K_S $(L/mg)^{1/m}$ is the Sips constant, related to energy of adsorption, and m is a dimensionless parameter characterising the system heterogeneity.

The equation of Brouers-Sotolongo model (Brouers et al., 2005) reads:

$$Q_e = Q_m \left(1 - exp\left(-K_w . C_e^{(a)}\right)\right) \quad (13)$$

where K_w (L/mg) is the Brouers constant and a (dimensionless) gives an indication of the adsorption energy heterogeneity of the surface.

The parameters of kinetic and isotherm models were determined by non-linear fitting using the Levenberg-Marquardt iteration algorithm supplied with the OriginPro® 2018 software.

3. Results and discussion

3.1. Elemental analysis and yields

Table 1 summarises the elemental analysis of all the materials studied here: raw Corn Stigmata (CS), hydrochar (HCS), carbon obtained by direct pyrolysis (CCS), carbonised hydrochar (CHCS), and ACs produced at different activation times of 0.5, 1, 2 and 3 h.

Table 1: Elemental composition (wt. %) and total yield of the materials.

Samples	C	H	N (wt. %)	S	O	Y_T (%)
Raw CS	48.06	6.31	3.07	0.27	41.53	-
Direct pyrolysis series						
CCS	82.56	0.77	3.42	0.16	7.86	25
AC0.5_CCS	76.65	1.77	2.95	0.24	13.84	14.55
AC1_CCS	72.93	2.11	3.14	0.31	15.69	6.83
AC2_CCS	3.89*	0.13	0.11	1.24	10.69	2.29
HTC series						
HCS	56.27	6.07	2.59	0.15	33.22	57
CHCS	88.64	0.61	2.57	0.12	4.88	30
AC1_CHCS	84.84	0.67	2.91	0.19	5.62	12.14
AC2_CHCS	82.71	0.63	2.83	0.34	5.83	7.35
AC3_CHCS	82.53	1.63	2.73	0.53	12.03	6.49

* The very low C content is due to a too long activation, which turned the major part of the sample into ashes (see Fig 1b).

256 The total of C, H, O, N and S contents was always lower than 100% due to the presence of
257 ashes. The elemental compositions of these materials were in the range of those found in the
258 literature (Selmi et al., 2018a). Raw CS has a carbon content of 48.1 wt. %, and a very high
259 oxygen content, 41.5 wt. %, typical of biomasses with a low lignin content. The ash content of
260 CS, determined by ASTM E1755, was 0.9 %. The latter is in excellent agreement with what
261 can be deduced by adding the C, H, O, N and S contents listed in the first row of Table 1: the
262 difference to 100% corresponds exactly to the measured ash content. This further supports our
263 claim that the sum of element contents is never equal to 100% due to the presence of ashes.
264 HTC of CS produced a slight enrichment in C with respect to CS, from 48.1 to 56.3 wt. %,
265 and a corresponding decrease of O content, from 41.5 to 33.2 wt. %. The pyrolysis increased
266 the C content of the final materials but still CHCS was richer in C than CCS, 88.64 against
267 82.56 wt. %, respectively. Indeed, CHCS presented lower contents of H, N, S, O and ashes
268 than CCS. After activation, the higher C content of CHCS was maintained when compared to
269 ACs derived from CCS. Increasing the activation time from 0.5 to 3h produced a decrease of
270 C content in both ACs series, and a corresponding increase of O and H contents.
271 Figure 1a shows the effect of activation time on the total carbon yield, Y_T, for both series of
272 materials (ACt_CHCS and ACt_CCS). Increasing the activation time produced the decrease
273 of Y_T because of the partial gasification of the precursor. The yield of the series submitted to
274 HTC, ACt_CHCS, remained always higher than that of non-pre-treated materials at the same
275 activation time. For example, the Y_T values of AC1_CHCS and AC1_CCS were 12.1 and 6.8
276 %, respectively. At 2 hours of activation, Y_T of AC2_CHCS was 3 times higher than that of
277 AC2_CCS, 7.4 and 2.3 %, respectively. In fact, AC2_CCS can no more be called an activated
278 carbon since mostly ashes were recovered (around 84 wt. %, according to Table 1), as
279 evidenced by the whitish colour of the as-obtained material (see Figure 1b) and by the very
280 low C content presented in Table 1, 3.9 wt. %. This fact clearly shows the importance of the

281 HTC step for the stabilisation of the structure since the materials from the HTC series are
282 much more resistant to activation, probably due to the higher aromatisation of CHCS with
283 respect to CCS. Consequently, activation of HTC-treated materials is slower and can be better
284 controlled.
285
286 **Figure 1: (a) Effect of activation time on the total yield Y_T; and (b) photo of AC2_CCS.**
287
288
289 **3.2. Textural properties**
290 The adsorption-desorption isotherms of N_2 at -196°C and of CO_2 at 0°C for CCS, CHCS and
291 their derived ACs are shown in Figure 2, as well as their corresponding pore size distributions
292 (PSDs). For all the materials, the nitrogen uptake (see Figure 2a and 2b) increased with the
293 relative pressure dramatically faster below $P/P_0 = 0.05$ than above, indicating the essentially
294 microporous nature of these carbon materials. As the activation time increased, the elbow of
295 the isotherm widened, demonstrating a broadening of the PSD in the microporous range. At
296 $P/P_0 > 0.1$, a pseudo-plateau was attained for CCS and CHCS materials, while a slightly
297 higher slope was observed for ACs, suggesting a multilayer adsorption due to the presence of
298 mesopores.
299 CCS exhibited a type Ia isotherm according to the IUPAC classification (IUPAC, 2015),
300 typical of ultramicroporous materials with adsorption occurring by primary filling of
301 micropores at very low relative pressure. The N_2 isotherms of AC0.5_CCS and AC1_CCS
302 materials were type IIb, with high uptake at low P/P_0, and a well-developed, type H4
303 hysteresis loop, indicating the simultaneous presence of wide micropores and mesopores. The
304 increase of activation time of CCS series significantly increased the porosity of the samples,
305 except for AC2_CCS, which was almost completely converted into ashes.

306 CHCS and ACt_CHCS exhibited N_2 adsorption isotherms of type Ib, showing the
307 existence of supermicroporosity (pores in the width range 0.7 – 2 nm), again with hysteresis
308 loop type H4 (Thommes et al., 2015) due to coexisting micro- and mesopores. Similar results
309 were found for ACs prepared from Agave Americana by HTC followed by physical activation
310 (Selmi et al., 2018a). While CCS and CHCS were essentially ultramicroporous (pore widths <
311 0.5 nm), their derived ACs presented an important fraction of supermicropores.
312 Figure 2c and Figure 2d show CO_2 adsorption at 0°C for CCS- and CHCS-derived carbons,
313 respectively. As CO_2 adsorption gives information on the narrow porosity, namely of width
314 less than 1.1 nm, these figures show that CCS has a more developed narrow porosity than
315 CHCS. It also shows that the activation was more effective for the materials derived from
316 CHCS, as the porosity that they developed was always higher than that of activated CCS
317 materials. Little differences of CO_2 adsorption were observed among ACt-CHCS materials,
318 indicating that the different activation times primarily affected the development of wide
319 micropores (wider than 1.1 nm) and mesopores.
320 Figure 2e and Figure 2f show the pore size distribution (PSD), in the micropore range,
321 calculated by application of the 2D-NLDFT model to both N_2 and CO_2 isotherms. These
322 results confirm that CCS was essentially ultramicroporous while CHCS possessed also
323 supermicropores. Increasing the activation time produced a broadening of the pores, except
324 for AC2_CCS, which presented only ultramicropores because the carbon content almost
325 totally vanished. In this particular case, it would have been probably better to use the 2D-
326 NLDFT model developed for cylindrical pores, instead of the one developed for slit-shaped
327 pores and which is more relevant to carbon materials. However, considering the very low
328 porosity of the resultant material, the difference between the results is expected to be
329 negligible.
330

Figure 2: (a,b) N_2 adsorption-desorption isotherms at -196°C; and (c,d) CO_2 adsorption-desorption isotherms at 0°C for CCS, CHCS and their derived ACs; and (e,f) their corresponding PSDs.

Figure 3 shows the changes of BET and NLDFT surface areas (A_{BET} and S_{NLDFT}, respectively), and micro-, meso- and total pore volumes (V_{micro}, V_{meso} and $V_{T,\ NLDFT}$, respectively) as a function of $1 - Y_T$. The latter quantity would indeed correspond to what is known as "burn-off" if only an activation process had been applied. Here, $1 - Y_T$ has a more general meaning, since it also takes into account the carbon that has been lost during the former steps of pyrolysis and HTC pre-treatment, if any. In all figures, an optimum was observed for both series of materials, i.e., with or without HTC pre-treatment. This indicates that the porosity primarily develops rather by broadening of pre-existing pores than by the creation of new ones. As a result, micropores grow and progressively become mesopores at higher activation time.

Figure 3d shows how the fraction of mesopores changes with $1 - Y_T$. CCS and CHCS series followed opposite trends. For similar values of $1 - Y_T$, CHCS-derived ACs always presented the highest fractions of mesoporosity and the highest mesopore volumes (except the too much activated A2_CCS, which is not representative of a normal AC), see Table 2. This finding is due to the hydrothermal treatment that essentially decomposes celluloses and hemicelluloses and preserves the lignin backbone as explained in the introduction, thus HTC leads to broader pores after pyrolysis. CHCS had also a much higher micropore volume, 0.12 cm^3/g, than CCS, 0.09 cm^3/g (Borrero-López et al., 2018; Jain et al., 2016).

The textural characteristics are summarised in Table 2. AC2_CHCS had higher A_{BET} and S_{NLDFT} than AC3_CHCS due to the broadening of micropores and the conversion of part of them into mesopores at 3 h of activation, as seen by the increase of mesopore fraction from 26

356 to 29 %. Thus, AC2_CHCS had the highest specific surface area out of all present ACs, as
357 also clearly seen in Figure 3a and Figure 3b.

358 From practical and economical points of view, as important as A_{BET} is the material yield,
359 Y_T (%). Table 2 gives also the values of A_{Tot} defined in Equation 2, taking into account both
360 A_{BET} and Y_T. ACs prepared from CHCS had always higher A_{Tot} than those prepared from
361 CCS. We chose AC2_CHCS because it presents the highest A_{Tot}, 81.7 m^2/g.

362

363 **Figure 3: Surface areas: (a) A_{BET}, and (b) S_{NLDFT}; (c) total volume (full symbols) and**
364 **micropore volume (empty symbols) and (d) fraction of mesoporosity as a function of (1 –**
365 **Y_T) for CCS and CHCS series. The lines are just guides for the eye.**

366

367 Table 2 also shows $V_{DR,N2}$ and $V_{DR,CO2}$, which give an estimation of the total micropore
368 volume and narrow micropore volume (pores narrower than 1.1 nm), respectively, determined
369 by the Dubinin-Raduskevich (DR) method (Dubinin, 1989). These parameters are given not
370 only for literature comparison purposes, but also because they give some insight about the
371 pores accessibility. Indeed, $V_{DR,N2} < V_{DR,CO2}$ indicates that narrow porosity, under 0.5 nm,
372 exists. This very narrow porosity is not accessible to nitrogen at -196°C, at the used
373 equilibrium times, but it is accessible to CO_2 at 0°C. CO_2 has a slightly higher cross-section
374 area (0.195 nm^2) than N_2 (0.162 nm^2), but the former diffuses in the narrowest pores due to
375 the higher temperature used. On the contrary, finding $V_{DR,N2} > V_{DR,CO2}$ indicates that the pore
376 texture is well developed and that the porous surface is more accessible to pollutants during
377 adsorption processes, as in the cases of A1_CCS, A2_CHCS and A3_CHCS. We consider
378 that $V_{mic,\ NLDFT}$ gives a more accurate estimation of the micropore volume, given that the DR
379 method generally overestimates micropore volumes for well-developed pore textures.

Table 2 also reports the values of $V_{0.97}$ and $V_{T, NLDFT}$. Usually, $V_{0.97}$ is lower than $V_{T, NLDFT}$ because the former only considers nitrogen adsorption while the latter considers also CO_2 adsorption. $V_{0.97}$ is given herein for literature comparison purposes.

Table 2: Textural properties of activated carbons.

	A_{BET} (m^2/g)	S_{NLDFT} (m^2/g)	A_{Tot} (m^2/g)	$V_{DR,N2}$ (cm^3/g)	$V_{DR,CO2}$ (cm^3/g)	$V_{0.97}$ (cm^3/g)	$V_{mic, NLDFT}$ (cm^3/g)	$V_{meso, NLDFT}$ (cm^3/g)	$V_{T, NLDFT}$ (cm^3/g)
CCS	47	498	11.8	0.02	0.14	0.03	0.09	0.01 (13%)	0.11
AC0.5_CCS	555	862	80.8	0.21	0.22	0.29	0.24	0.08 (24%)	0.31
AC1_CCS	838	940	57.2	0.31	0.24	0.33	0.25	0.08 (23%)	0.33
AC2_CCS	43	67	1.0	0.01	0.06	0.05	0.01	0.06 (83%)	0.07
CHCS	188	514	56.4	0.08	0.13	0.13	0.12	0.07 (38%)	0.19
AC1_CHCS	660	1046	80.1	0.25	0.30	0.36	0.28	0.12 (29%)	0.39
AC2_CHCS	1111	1273	81.7	0.42	0.06	0.56	0.42	0.14 (26%)	0.56
AC3_CHCS	1000	1183	64.9	0.38	0.32	0.52	0.38	0.15 (29%)	0.53

Scanning electron microscopy studies were carried out to show the development of porosity and the characteristics of the surface of AC2_CHCS in comparison to those of CHCS and CS, see Figure 4. The surface morphology of raw CS presented an uneven and apparently non–porous surface at such magnification. The hydrothermally treated material was visibly much more porous, with a rather rough surface. This observation corroborates its low A_{BET} of 188 m^2/g. It can also be seen that the fibrous nature of the precursor was preserved in CS and CHCS, see Figure 4a and Figure 4b, respectively.

Figure 4c shows a zone of AC2_CHCS with several microspheres that are characteristic of hydrothermally treated cellulose. This observation is in agreement with what was already reported when different vegetal biomasses were submitted to HTC and/or HTC and pyrolysis (Laginhas et al., 2016; Selmi et al., 2018a; Sevilla et al., 2011; Tran et al., 2017). Obviously,

397 the effect of activation could not be observed when comparing Figure 4b and 4c because the
398 size of the pores that were produced is out of the range of what can be seen by SEM.
399
400 **Figure 4: SEM images of: (a) CS; (b) CHCS; and (c) AC2_CHCS.**
401
402 **3.3. Surface characterisation of AC2_CHCS**
403 Given that AC2_CHCS had the highest S_{NLDFT}, this material was chosen for subsequent
404 MB adsorption tests. A deeper characterisation of the functional groups of the latter material
405 was carried out to better explain and discuss its MB adsorption performances.
406 Figure 5a shows that the pH_{PZC} of AC2_CHCS was equal to 8.6. Therefore, at pH > 8.6,
407 the AC surface is negatively charged and the adsorption of the MB, which is a cationic dye, is
408 expected to be favourable. Figure 5b shows the results of the potentiometric titration of
409 AC2_CHCS. Five peaks were found at pK_a equal to 3.24, 5.06, 6.57, 7.33 and 9.75. The total
410 amounts of acidic and basic groups were 0.550 mmol/g and 0.743 mmol/g, respectively.
411 AC2_CHCS is thus characterised by a basic surface in agreement with its pH_{PZC} equal to 8.6.
412 Following the classification proposed elsewhere, the groups with $pK_a < 8$ are assumed to be
413 carboxyls, and those with $pK_a > 8$ are classified as phenols and quinones (Bandosz et al.,
414 1993).
415
416 **Figure 5: (a) Point of zero charge; and (b) pK_a and amounts of surface groups**
417 **determined by potentiometric titration of AC2_CHCS.**
418
419 Figure 6a shows the Fourier-transform infrared (FTIR) spectra of CS and CHCS. The
420 surface chemistry of CS is relatively similar to that of other types of lignocellulosic materials,
421 which are essentially composed of cellulose, hemicellulose and lignin (Xu et al., 2013). The

CHCS spectrum had a general shape similar to that of CS, with a slight shift of the 3421 cm^{-1} band characteristic of O-H stretching of lignin to 3364 cm^{-1}, respectively. Bands at 2916 and 2849 cm^{-1} are characteristic of C-H stretching and were obviously present in both materials (Mahmoudi et al., 2012). Figure 6b shows FTIR spectra of AC2_CHCS before and after MB adsorption. Overall, the ACs showed a dramatic decrease in the intensity of all bands with respect to their carbonaceous precursors shown in Figure 6a, suggesting an increase of aromaticity due to the carbonisation at 900°C (Bouchelta et al., 2008), and hence a corresponding loss of surface functions. After MB adsorption, IR bands exhibited slight changes, suggesting the involvement of several moieties. Especially, the decrease of the band at 1551 cm^{-1} and the appearance of that at 1383 cm^{-1} suggest π - π interaction between the carbon surface and MB, and the presence of aromatic amines after adsorption due to the presence of MB, respectively.

Figure 6: FTIR spectra of: (a) CS and CHCS; and (b) activated carbon (AC2_CHCS) before and after MB adsorption.

3.4. MB adsorption

3.4.1. Effect of pH and temperature, and thermodynamic studies

Selected isotherms were repeated three times, based on which a relative error of less than 5% was observed. Figure 7 illustrates the effect of pH and temperature on the MB adsorption capacity of AC2_CHCS. Figure 7a shows that the MB adsorption capacity of AC2_CHCS increased considerably when the solution pH increased from 2 to 6. The maximum MB uptake was obtained at pH 7, and remained approximately constant between 7 and 10, indicating that MB adsorption in basic medium was not significantly influenced by the pH. Such results are logical considering that, at pH equal to 2 or 4, the material surface is positively charged so

447 that the cationic dye MB is not favourably adsorbed. However, π - π interactions were likely
448 to occur, as suggested by the fact that the uptake was still high at pH slightly below the pH_{PZC}.
449 Indeed, when the pH increased to 7, the surface charge was still somewhat globally positively
450 charged since the pH_{PZC} is 8.3. At even higher pH, the number of negatively charged sites on
451 the AC surface was the highest, thus favouring the electrostatic attraction between the AC
452 surface and MB.

453 In order to understand the thermodynamic behaviour of MB adsorption onto AC2_CHCS,
454 the effect of temperature on MB adsorption was investigated in the range of 20 to 40°C, at
455 initial MB concentrations of 10, 40 and 100 mg/L. Figure 7b shows that MB adsorption
456 capacity increased with temperature and initial concentration. The values of the
457 thermodynamic parameters for MB adsorption onto AC2_CHCS are summarised in Table 3.

458

459 **Figure 7: Effect on the MB adsorption capacity of AC2_CHCS of: (a) pH (at 25°C and**
460 **C_0 = 10 mg/L); and (b) C_0 and temperature (at pH 10).**

461
462 Table 3: Thermodynamic parameters for the adsorption of MB onto AC2_CHCS at different
463 temperatures and three initial MB concentrations.

Concentration (mg/L)	$\Delta H°$ (kJ/mol)	$\Delta S°$ (J /mol/K)	$\Delta G°$ (kJ/mol)		
			20°C	30°C	40°C
10	49.23	178.16	-3.03	-4.62	-6.60
40	70.31	225.32	-4.67	-6.67	-9.80
100	84.73	305.53	-4.90	-7.61	-11.03

464
465 $\Delta G°$ values were all negative, at the three initial concentrations and for the three selected
466 temperatures, confirming the spontaneous nature of MB adsorption onto AC2_CHCS.
467 Although $\Delta H°$ values were positive, in agreement with previous studies (Enaime et al., 2017),
468 adsorption was possible due to the positive values of $\Delta S°$, indicating an increased randomness

469 at the solid-solution interface during MB adsorption (Selmi et al., 2018d). $\Delta H°$ and $\Delta S°$ both
470 increased when increasing the MB concentration from 10 to 100 mg/L. Furthermore, the
471 increase with temperature of the absolute values of $\Delta G°$ supported the better adsorption at
472 higher temperatures, in agreement with previous studies (Moyo et al., 2013).
473
474 **3.4.2. Kinetic studies**
475 The fits to the PFO, PSO, and BSf models were evaluated based on the values of
476 determination coefficient (R^2) and of non-linear chi-square (χ^2) parameter. Statistical data at
477 three different initial concentrations (10, 20 and 100 mg/L) of MB at 25°C are presented in
478 Table 4.
479 The application of the BSf model led to the highest and lowest values of R^2 and χ^2,
480 respectively. The maximum adsorption values for all concentrations determined by the BSf
481 model, Q_{eBS}, (10.6, 20.1 and 96.6 mg/g) were those approaching most the experimental ones,
482 Q_e (10.5; 20.08 and 97.01 mg/g). Therefore, the BSf model is the most suitable model for
483 describing the kinetic adsorption of MB on AC2_CHCS, suggesting that this process is fractal
484 because of the surface and interface heterogeneity that can be of chemical and/or topological
485 origin. Chemical heterogeneity is due to the existence of various surface functions, as proved
486 by potentiometric titration, while topological heterogeneity, consisting in different pore
487 diameters, was evidenced by nitrogen and carbon dioxide adsorption that allowed the
488 calculation of the PSDs. Moreover, the fractal character of MB adsorption on AC2_CHCS
489 was also confirmed by the values of the "fractional times" α, which were always lower than 1,
490 in agreement with previous results (Kesraoui et al., 2017; Selmi et al., 2018c). When the
491 concentration increased from 10 to 100 mg/L, the fractality increased as well, as suggested by
492 the decrease of the values of α from 0.614 to 0.49, again in agreement with former studies
493 (Selmi et al., 2018b). The n parameter of BSf, which is the non-integer reaction order, was

494 always lower than 1 (between 0.517 and 0.797 for 10 and 100 mg/L, respectively), also in
495 agreement with previous works (Selmi et al., 2018c; Selmi et al., 2018d). The increase of *n*
496 with the concentration is related to diffusion phenomena, indicating that MB adsorption
497 became faster when the initial MB concentration was increased. This finding is supported by
498 the characteristic time, τ_c, which decreased when the MB concentration increased.
499
500 Table 4: Kinetic parameters derived from the nonlinear fits of three of the selected kinetic
501 models to the experimental data.

Parameters	Initial MB concentration (mg/L)		
	10	20	100
Experimental Q_e (mg/g)	10.50	20.08	97.01
Pseudo-first-order (PSO)			
Q_{e1} (mg/g)	10.71	19.87	95.37
k_1 (1/min)	0.153	0.277	0.328
R^2	0.994	0.998	0.997
χ^2	0.094	0.148	3.065
Pseudo-second-order (PSO)			
Q_{e2} (mg/g)	12.88	21.92	100.46
k_2 (mg/g/min)	0.013	0.021	0.007
R^2	0.996	0.999	0.999
χ^2	0.056	0.074	0.996
Brouers-Sotolongo fractal (BSf)			
$Q_{e,BS}$ (mg/g)	10.683	20.142	96.608
n	0.517	0.634	0.797
α	0.614	0.508	0.493
τ_c (min)	9.204	4.164	2.492
R^2	0.998	0.999	0.999
χ^2	0.043	0.021	0.395

502
503

3.4.3. Isotherms studies

Figure 8 shows the experimental adsorption data fitted by the four isotherm models: Langmuir, Freundlich, Sips and BS. The corresponding adsorption parameters are presented in Table 5.

Figure 8: Nonlinear fit of MB isotherm adsorption of AC2_CHCS at pH 10 and 25°C.

Table 5: Adsorption isotherm constants for MB adsorption onto AC2_CHCS.

Isotherm model	**MB Parameters**
Experimental Q_m (mg/g)	561.5
Langmuir	
Q_m (mg/g)	871.3
K_L	0.074
R^2	0.9988
χ^2	50.150
Freundlich	
K_F	82.148
n	1.626
R^2	0.9799
χ^2	887.032
Sips	
Q_m (mg/g)	805.3
K_S ((L/mg)$^{1/m}$)	0.116
m	1.214
R^2	0.9998
χ^2	9.728
Brouers-Sotolongo (BS)	
Q_m (mg/g)	607.2
K_w (L/mg)	0.094
a	1.024
R^2	0.9999
χ^2	3.022

Based on the determination coefficients found for each model, the BS and Sips models appeared as the most appropriate ones to fit the experimental data, with R^2 values as high as

515 0.9999 and 0.9998, respectively. Moreover, the very high values of χ^2 found for both
516 Langmuir and Freundlich models indicated their irrelevance for describing correctly the
517 equilibrium data. Langmuir and Sips models also led to calculated Q_e values (871.3 and 805.2
518 mg/g, respectively) in poor agreement with the experimental Q_e one (561.5 mg/g).

519 In contrast, the Q_m value obtained from Brouers-Sotolongo isotherm, 607.2 mg/g, was the
520 closest to the experimental one, in complete agreement with the lowest value of χ^2 observed
521 for the fit. Therefore, the BS isotherm was the most adequate for describing the adsorption of
522 MB onto AC2_CHCS, compared to Freundlich, Langmuir and Sips isotherms. BS model
523 assumes strong interactions between MB and the AC, due to the high heterogeneity of the
524 surface groups, namely carbonyls, phenols and lactones, confirmed by the value of the *a*
525 parameter, which is higher than 1. Similar results were found in previous studies (Selmi et al.,
526 2018a; Selmi et al., 2018c; Selmi et al., 2018d).

527

528 **3.4.4. Comparison with literature data**

529 Table 6 shows the maximum MB adsorption capacities obtained by ACs prepared from
530 various biomasses by HTC and subsequent pyrolysis. In the present work, the maximum MB
531 adsorption, Q_e, was 561.5 mg/g, higher than that of several activated carbons reported in the
532 literature (Islam et al., 2017; Sanja et al., 2018; Tong et al., 2018). An almost linear
533 relationship between Q_e and A_{BET} was observed (not shown). Thus, the highest Q_e was found
534 with cluster stalks-derived AC (Alcaraz et al., 2018) with A_{BET} equal to 2662 m^2/g and
535 produced by KOH activation. Although the area was very high, it is necessary to take into
536 account the time and the high amount of water used for washing samples prepared by
537 chemical activation, and that KOH is highly corrosive and even potentially harmful for
538 equipment and operators. Unexpectedly low MB adsorption was obtained when using
539 glucose-derived AC, with a value of Q_e of only 61.0 mg/g, although this material had an A_{BET}

of 1357 m^2/g, i.e., slightly higher than that of AC2_CHCS, which cannot be easily explained without more information about this material.

Table 6: MB removal efficiencies of ACs produced from different biomasses.

AC precursor	A_{BET} (m^2/g)	C_0 (mg/L)	Adsorbent dose (g/L)	T (°C)	pH	Q_e (mg/g)	Reference
cluster stalks	2662	50	0.2	30	7	925.9	(Alcaraz et al., 2018)
bagasse	1861	50	0.2	30	7	714.3	
walnut shells	1800	2000	4	25	-	315	(Yang and Qiu, 2010)
Mangosteen peel waste	1621	500	0.3	25	9	1193	(Nasrullah et al., 2019)
sucrose	1534	900	0.8	25	5.5	704.2	(Bedin et al., 2016)
glucose	1357	200	1	25	6.6	61.0	(Sanja et al., 2018)
fructose	701	200	1	25	6.6	197.0	
Acacia mangium wood	1161	329	2	27	-	159.89	(Danish et al., 2018a)
banana trunk waste	1173	250	1.5	25	-	166.51	(Danish et al., 2018b)
coconut shells	876	250	1	30	7	200.01	(Islam et al., 2017)
cellulose/montmorillonite	42	160	1	25	8	138.1	(Tong et al., 2018)
Corn stigmata	1111	650	1	25	10	561.5	This study

4. Conclusion

The objective of the present study was to show, for the first time, the effect of a preliminary hydrothermal carbonisation (HTC) step in the preparation of CO_2-activated carbons (ACs) from Corn Stigmata (CS) fibres. It was found that the preliminary HTC step allowed recovering activated carbons with higher yields, higher carbon contents, and more developed porous textures. The activation was also slower, thus allowing a better control of the process. The material having the highest surface area, 1111 m^2/g, was then investigated in detail. Its pH at point of zero charge was found to be 8.6, and its surface was found to be mainly basic, with a total amount of basic groups of 0.743 mmol/g against 0.550 mmol/g for acidic groups.

These characteristics were quite favourable for adsorbing MB, which is a cationic dye. In the temperature range from 20 to 40°C, MB adsorption was shown to be spontaneous and endothermic, as proved by the corresponding calculated thermodynamic parameters ($\Delta G°$= -4.90 kJ/mol and $\Delta H°$ = 84.73 kJ/mol at 20°C). The uptake increased with the pH, as expected, and was the highest and almost constant above pH 7. Both the isotherms at equilibrium and the kinetic data were best fitted by the Brouers-Sotolongo model, suggesting the fractal character of MB adsorption on such very heterogeneous surfaces. MB uptakes as high as 561.5 mg/g were measured at 25°C, indicating the excellent adsorption properties of such materials for retaining toxic dyes. Overall, the hydrochars produced from CS were thus proved effective precursors of ACs for water remediation.

Acknowledgements

The authors gratefully acknowledge the financial support from the Tunisian Ministry of Higher Education and Scientific Research. This study was partly supported by TALiSMAN project, funded by FEDER (2019-000214).

571 **References**

572 Acosta, R., Nabarlatz, D., Sánchez-Sánchez, A., Jagiello, J., Gadonneix, P., Celzard, A.,
573 Fierro, V., 2018. Adsorption of Bisphenol A on KOH-activated tyre pyrolysis char. J Environ
574 Chem Eng 6, 823-833.
575 Alcaraz, L., Fernández, A.L., Garcia-Díaz, I., López, F., 2018. Preparation and
576 characterization of activated carbons from winemaking wastes and their adsorption of
577 methylene blue. Adsor Sci Technol 0, 1-21.
578 Altenor, S., Ncibi, M.C., Emmanuel, E., Gaspard, S., 2012. Textural characteristics,
579 physiochemical properties and adsorption efficiencies of Caribbean alga Turbinaria turbinata
580 and its derived carbonaceous materials for water treatment application. Biochem Eng J 67, 35-
581 44.
582 Bandosz, T.J., Jagiello, J., Contescu, C., Schwarz, J.A., 1993. Characterization of the surfaces
583 of activated carbons in terms of their acidity constant distributions. Carbon 31, 1193-1202.
584 Basso, D., Weiss-Hortala, E., Patuzzi, F., Castello, D., Baratieri, M., Fiori, L., 2015.
585 Hydrothermal carbonization of off-specification compost: A byproduct of the organic
586 municipal solid waste treatment. Bioresource Technol. 182, 217-224.
587 Bedin, K.C., Martins, A.C., Cazetta, A.L., Pezoti, O., Almeida, V.C., 2016. KOH-activated
588 carbon prepared from sucrose spherical carbon: Adsorption equilibrium, kinetic and
589 thermodynamic studies for Methylene Blue removal. Chem Eng J 286, 476-484.
590 Borrero-López, A.M., Fierro, V., Jeder, A., Ouederni, A., Masson, E., Celzard, A., 2017. High
591 added-value products from the hydrothermal carbonisation of olive stones. Environ Sci Pollut
592 Res 24, 9859-9869.
593 Borrero-López, A.M., Masson, E., Celzard, A., Fierro, V., 2018. Modelling the reactions of
594 cellulose, hemicellulose and lignin submitted to hydrothermal treatment. Ind Crops Prod 124,
595 919-930.
596 Bouchelta, C., Medjram, M.S., Bertrand, O., Bellat, J.-P., 2008. Preparation and
597 characterization of activated carbon from date stones by physical activation with steam. J
598 Anal Appl Pyrol. 82, 70-77.
599 Braghiroli, F.L., Fierro, V., Izquierdo, M.T., Parmentier, J., Pizzi, A., Celzard, A., 2012.
600 Nitrogen-doped carbon materials produced from hydrothermally treated tannin. Carbon 50,
601 5411-5420.

602 Braghiroli, F.L., Fierro, V., Izquierdo, M.T., Parmentier, J., Pizzi, A., Celzard, A., 2014.
603 Kinetics of the hydrothermal treatment of tannin for producing carbonaceousmicrospheres.
604 Bioresource Technol. 151, 271–277.
605 Braghiroli, F.L., Fierro, V., Izquierdo, M.T., Parmentier, J., Pizzi, A., Delmotte, L., Fioux, P.,
606 Celzard, A., 2015. High surface – Highly N-doped carbons from hydrothermally treated
607 tannin. Ind Crops Prod 66, 282-290.
608 Brouers, F., Sotolongo-Costa, O., 2006. Generalized fractal kinetics in complex systems
609 (application to biophysics and biotechnology). Phys A: Stat Mech Appl 368, 165-175.
610 Brouers, F., Sotolongo, O., Marquez, F., Pirard, J.P., 2005. Microporous and heterogeneous
611 surface adsorption isotherms arising from Levy distributions. Phys A: Stat Mech Appl 349,
612 271-282.
613 Danish, M., Ahmad, T., Hashim, R., Said, N., Akhtar, M.N., Mohamad-Saleh, J., Sulaiman,
614 O., 2018a. Comparison of surface properties of wood biomass activated carbons and their
615 application against rhodamine B and methylene blue dye. Surfaces and Interfaces 11, 1-13.
616 Danish, M., Ahmad, T., Majeed, S., Ahmad, M., Ziyang, L., Pin, Z., Shakeel Iqubal, S.M.,
617 2018b. Use of banana trunk waste as activated carbon in scavenging methylene blue dye:
618 Kinetic, thermodynamic, and isotherm studies. Bioresource Technology Reports 3, 127-137.
619 Dubinin, M.M., 1989. Fundamentals Of The Theory Of Adsorption In Micropores Of Carbon
620 Adsorbents: Characteristics Of Their Adsorption Properties And Microporous Structures.
621 Carbon 27, 457-567.
622 Enaime, G., Ennaciri, K., Ounas, A., Baçaoui, A., Seffen, M., Selmi, T., Yaacoubi, A., 2017.
623 Preparation and characterization of activated carbons from olive wastes by physical and
624 chemical activation: Application to Indigo carmine adsorption. J Mater Environ Sci 8, 4125-
625 4137.
626 Fierro, V., Muñiz, G., Basta, A.H., El-Saied, H., Celzard, A., 2010. Rice straw as precursor of
627 activated carbons: Activation with ortho-phosphoric acid. J Hazard Mater 181, 27-34.
628 Freundlich, H., 1906. Over the adsorption in solution. J Phys Chem 57, 385-471.
629 Gaspard, S., Altenor, S., Passe-Coutrin, N., Ouensanga, A., Brouers, F., 2006. Parameters
630 from a new kinetic equation to evaluate activated carbons efficiency for water treatment.
631 Water Res 40, 3467-3477.
632 Georgin, J., Dotto, G.L., Mazutti, M.A., Foletto, E.L., 2016. Preparation of activated carbon
633 from peanut shell by conventional pyrolysis and microwave irradiation-pyrolysis to remove
634 organic dyes from aqueous solutions. J Environ Chem Eng 4, 266-275.

635 Ghouma, I., Mejdi, J., Sophie, D., Lionel, L., Camelia, M.G., Abdelmottaleb, O., 2015.
636 Activated carbon prepared by physical activation of olive stones for the removal of NO_2 at
637 ambient temperature. Compt Rend Chim 18, 63–74.
638 Ho, Y.S., McKay, G., 1998. Sorption of dye from aqueous solution by peat. Chem Eng J 70,
639 115-124.
640 Ho, Y.S., McKay, G., 1999. Pseudo-second order model for sorption processes. Process
641 Biochem 34, 451-465.
642 Islam, M.A., Ahmed, M.J., Khanday, W.A., Asif, M., Hameed, B.H., 2017. Mesoporous
643 activated coconut shell-derived hydrochar prepared via hydrothermal carbonization-NaOH
644 activation for methylene blue adsorption. J Environ Manage 203, 237-244.
645 IUPAC, 2015. International Union of Pure and Applied Chemistry; Korean Chemical Society,
646 45th IUPAC World Chemestry Congress. Elseviers, Busan, Korea.
647 Jagiello, J., 1994. Stable Numerical Solution of the Adsorption Integral Equation Using
648 Splines. Langmuir 10, 2778-2785.
649 Jagiello, J., Bandosz, T.J., Putyera, K., Schwarz, J.A., 1995. Determination of proton affinity
650 distributions for chemical systems in aqueous environments using a stable numerical solution
651 of the adsorption intergral equation J Colloid Interface Sci 172, 341-346.
652 Jagiello, J., Kenvin, J., Celzard, A., Fierro, V., 2019. Enhanced resolution of ultra micropore
653 size determination of biochars and activated carbons by dual gas analysis using N2 and CO2
654 with 2D-NLDFT adsorption models. Carbon 144, 206-215.
655 Jain, A., Balasubramanian, R., Srinivasan, M.P., 2016. Hydrothermal conversion of biomass
656 waste to activated carbon with high porosity: A review. Chem Eng J 283, 789-805.
657 Jatzwauck, M., Schumpe, A., 2015. Kinetics of hydrothermal carbonization (HTC) of soft
658 rush. Biomass and Bioenergy 75, 94-100.
659 Kesraoui, A., Selmi, T., Seffen, M., Brouers, F., 2017. Influence of alternating current on the
660 adsorption of indigo carmine. Environ Sci Pollut Res 24, 9940-9950.
661 Lagergren, S., 1898. Zur Theorie der Sogenannten Adsorption Gelöster Stoffe, Kungliga
662 Svenska Vetenskapsakade- miens. Handlingar 24, 1-39.
663 Laginhas, C., Nabais, J.M.V., Titirici, M.M., 2016. Activated carbons with high nitrogen
664 content by a combination of hydrothermal carbonization with activation. Microporous
665 Mesoporous Mater 226, 125-132.
666 Langmuir, I., 1918. The adsorption of gases on plane surfaces of glass, mica, and platinum. J
667 American Chem Society 40, 1361.

668 Mahmoudi, K., Hamdi, N., Kriaa, A., Srasra, S., 2012. Adsorption of Methyl Orange Using
669 Activated Carbon Prepared from Lignin by ZnCl2 Treatment. Russian J Phys Chem A 86,
670 1294–1300.
671 Marsh, H., Rodríguez-Reinoso, F., 2006a. CHAPTER 5 - Activation Processes (Thermal or
672 Physical), in: Marsh, H., Rodríguez-Reinoso, F. (Eds.), Activated Carbon. Elsevier Science
673 Ltd, Oxford, pp. 243-321.
674 Marsh, H., Rodríguez-Reinoso, F., 2006b. CHAPTER 9 - Production and Reference Material,
675 in: Marsh, H., Rodríguez-Reinoso, F. (Eds.), Activated Carbon. Elsevier Science Ltd, Oxford,
676 pp. 454-508.
677 Mbarki, F., Kesraoui, A., Seffen, M., Ayrault, P., 2018. Kinetic, Thermodynamic, and
678 Adsorption Behavior of Cationic and Anionic Dyes onto Corn Stigmata: Nonlinear and
679 Stochastic Analyses. Water, Air, & Soil Pollution 229, 95.
680 Métivier-Pignon, H., Faur-Brasquet, C., Le Cloirec, P., 2003. Adsorption of dyes onto
681 activated carbon cloths: approach of adsorption mechanisms and coupling of ACC with
682 ultrafiltration to treat coloured wastewaters. Separation and Purification Technology 31, 3-11.
683 Moyo, M., Chikazaza, L., Nyamunda, B.C., Guyo, U., 2013. Adsorption Batch Studies on the
684 Removal of Pb(II) Using Maize Tassel Based Activated Carbon. Journal of Chemistry 2013,
685 8.
686 Nasrullah, A., Saad, B., Bhat, A.H., Khan, A.S., Danish, M., Isa, M.H., Naeem, A., 2019.
687 Mangosteen peel waste as a sustainable precursor for high surface area mesoporous activated
688 carbon: Characterization and application for methylene blue removal. J Clean Prod 211, 1190-
689 1200.
690 Olad, A., Amani-Ghadim, A.R., Dorraji, M.S.S., Rasoulifard, M.H., 2010. Removal of the
691 Alphazurine FG Dye from Simulated Solution by Electrocoagulation. CLEAN – Soil, Air,
692 Water 38, 401-408.
693 Podder, M.S., Majumder, C.B., 2016. Studies on the removal of As(III) and As(V) through
694 their adsorption onto granular activated carbon/MnFe2O4 composite: isotherm studies and
695 error analysis. Composite Interfaces 23, 327-372.
696 Sanja, K., Milan, K., Maja, P., Vladimir, D., Branka, K., Miloš, M., Ivica, R., Marija, S.,
697 2018. Hydrothermal Synthesized and Alkaline Activated Carbons Prepared from Glucose and
698 Fructose—Detailed Characterization and Testing in Heavy Metals and Methylene Blue
699 Removal. Minerals 8, 246.
700 Selmi, T., Sanchez-Sanchez, A., Gadonneix, P., Jagiello, J., Seffen, M., Sammouda, H.,
701 Celzard, A., Fierro, V., 2018a. Tetracycline removal with activated carbons produced by

hydrothermal carbonisation of Agave americana fibres and mimosa tannin. Ind Crops Prod 115, 146-157.

Selmi, T., Seffen, M., Brouers, F., Fierro, V., Sammouda, H., 2018b. Adsorption of Model Dyes Onto Porous Materials: Effect of pH and Temperature on the Parameters of Brouers-Sotolongo Kinetic Fractal and Generalized Isotherm, in: Kallel, A., Ksibi, M., Ben Dhia, H., Khélifi, N. (Eds.), Recent Advances in Environmental Science from the Euro-Mediterranean and Surrounding Regions: Proceedings of Euro-Mediterranean Conference for Environmental Integration (EMCEI-1), Tunisia 2017. Springer International Publishing, Cham, pp. 1039-1041.

Selmi, T., Seffen, M., Celzard, A., Fierro, V., 2018c. Effect of the adsorption pH and temperature on the parameters of the Brouers–Sotolongo models. Environ Sci Pollut Res 10, 1-10.

Selmi, T., Seffen, M., Sammouda, H., Sandrine, M., Jagiello, J., Celzard, A., Fierro, V., 2018d. Physical meaning of the parameters used in fractal kinetic and generalised adsorption models of Brouers–Sotolongo. Adsorption 24, 11-27.

Sevilla, M., Fuertes, A.B., 2009. Chemical and Structural Properties of Carbonaceous Products Obtained by Hydrothermal Carbonization of Saccharides. Chemistry – A European Journal 15, 4195-4203.

Sevilla, M., Maciá-Agulló, J.A., Fuertes, A.B., 2011. Hydrothermal carbonization of biomass as a route for the sequestration of CO2: Chemical and structural properties of the carbonized products. Biomass and Bioenergy 35, 3152-3159.

Sips, R., 1948. The Structure of a Catalyst Surface. J Chem Phys 16, 490-495.

Steinbeiss, S., Gleixner, G., Antonietti, M., 2009. Effect of biochar amendment on soil carbon balance and soil microbial activity. Soil Biology and Biochemistry 41, 1301-1310.

Thommes, M., Kaneko, K., Neimark Alexander, V., Olivier James, P., Rodriguez-Reinoso, F., Rouquerol, J., Sing Kenneth, S.W., 2015. Physisorption of gases, with special reference to the evaluation of surface area and pore size distribution (IUPAC Technical Report), Pure and Applied Chemistry, p. 1051.

Tong, D.S., Wu, C.W., Adebajo, M.O., Jin, G.C., Yu, W.H., Ji, S.F., Zhou, C.H., 2018. Adsorption of methylene blue from aqueous solution onto porous cellulose-derived carbon/montmorillonite nanocomposites. Applied Clay Science 161, 256-264.

Tran, H.N., You, S.-J., Nguyen, T.V., Chao, H.-P., 2017. Insight into the adsorption mechanism of cationic dye onto biosorbents derived from agricultural wastes. Chem Eng Comm 17, 1-17.

736 Xu, F., Yu, J., Tesso, T., Dowell, F., Wang, D., 2013. Qualitative and quantitative analysis of
737 lignocellulosic biomass using infrared techniques: A mini-review. Applied Energy 104, 801-
738 809.
739 Yang, J., Qiu, K., 2010. Preparation of activated carbons from walnut shells via vacuum
740 chemical activation and their application for methylene blue removal. Chem Eng J 165, 209-
741 217.
742 Zhou, H., Wu, C., Onwudili, J.A., Meng, A., Zhang, Y., Williams, P.T., 2014. Polycyclic
743 Aromatic Hydrocarbon Formation from the Pyrolysis/Gasification of Lignin at Different
744 Reaction Conditions. Energy & Fuels 28, 6371-6379.

745
746

747 # List of tables

756

Figure captions

Figure 1: (a) Effect of activation time on the total yield Y_T; and (b) photo of AC2_CCS. Lines in (a) are just guides for the eye.

Figure 2: (a,b) N_2 adsorption-desorption isotherms at -196°C; and (c,d) CO_2 adsorption-desorption isotherms at 0°C for CCS, CHCS and their derived ACs; and (e,f) their corresponding PSDs.

Figure 3: Surface areas: (a) A_{BET}, and (b) S_{NLDFT}; (c) total volume (full symbols) and micropore volume (empty symbols) and (d) fraction of mesoporosity as a function of $(1 - Y_T)$ for CCS and CHCS series. The lines are just guides for the eye.

Figure 4: SEM images of: (a) CS; (b) CHCS; and (c) AC2_CHCS.

Figure 5: (a) Point of zero charge; and (b) pK_a and amounts of surface groups determined by potentiometric titration of AC2_CHCS.

Figure 6: FTIR spectra of: (a) CS and CHCS; and (b) activated carbon (AC2_CHCS) before and after MB adsorption.

Figure 7: Effect on the MB adsorption capacity of AC2_CHCS of: (a) pH (at 25°C and C_0 = 10 mg/L); and (b) C_0 and temperature (at pH 10). The line in (a) is just a guide for the eye.

Figure 8 : Nonlinear fit of MB isotherm adsorption of AC2_CHCS at pH 10 and 25°C.

Figures

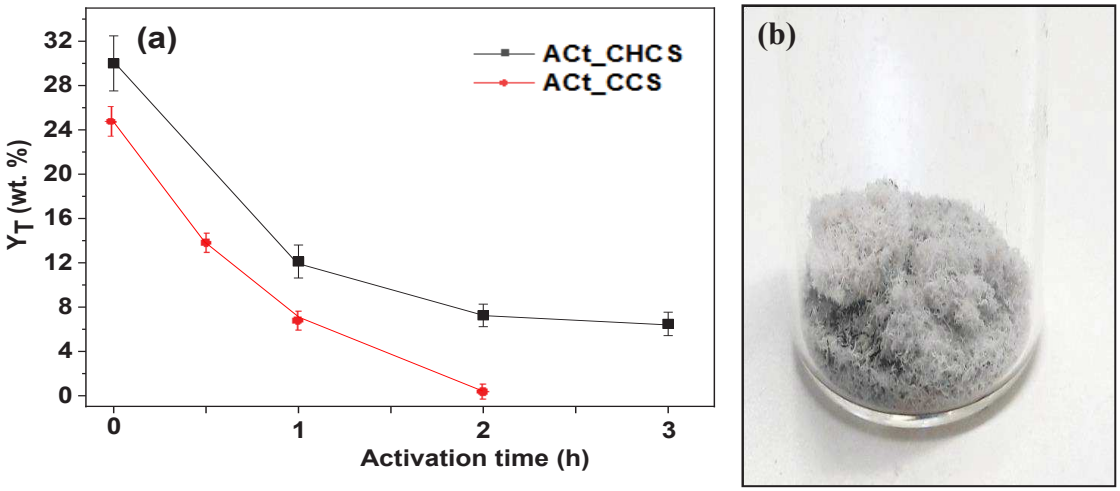

Figure 1: (a) Effect of activation time on the total yield Y_T; and (b) photo of AC2_CCS. Lines in (a) are just guides for the eye.

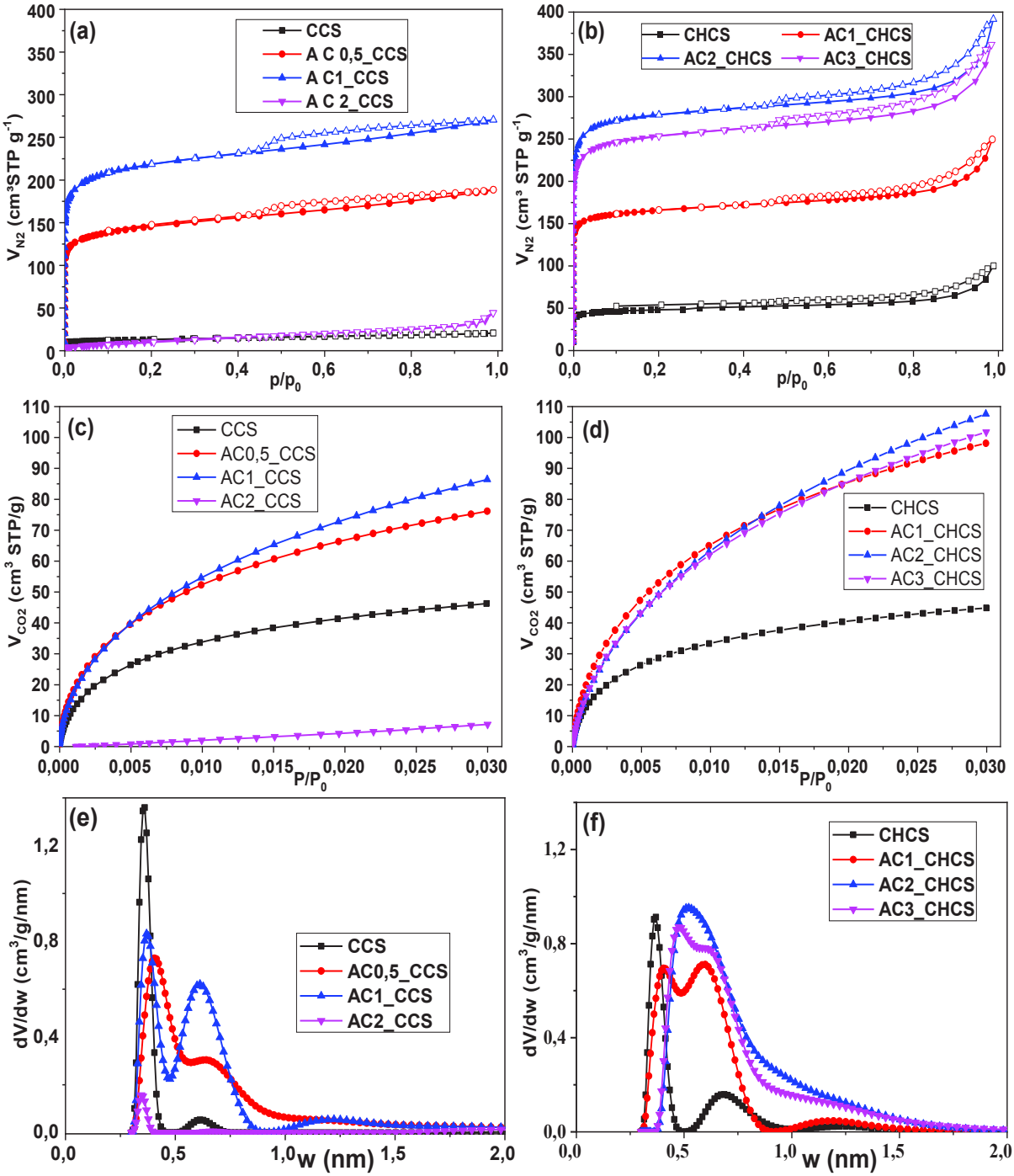

Figure 2: (a,b) N_2 adsorption-desorption isotherms at -196°C; and (c,d) CO_2 adsorption-desorption isotherms at 0°C for CCS, CHCS and their derived ACs; and (e,f) their corresponding PSDs.

790

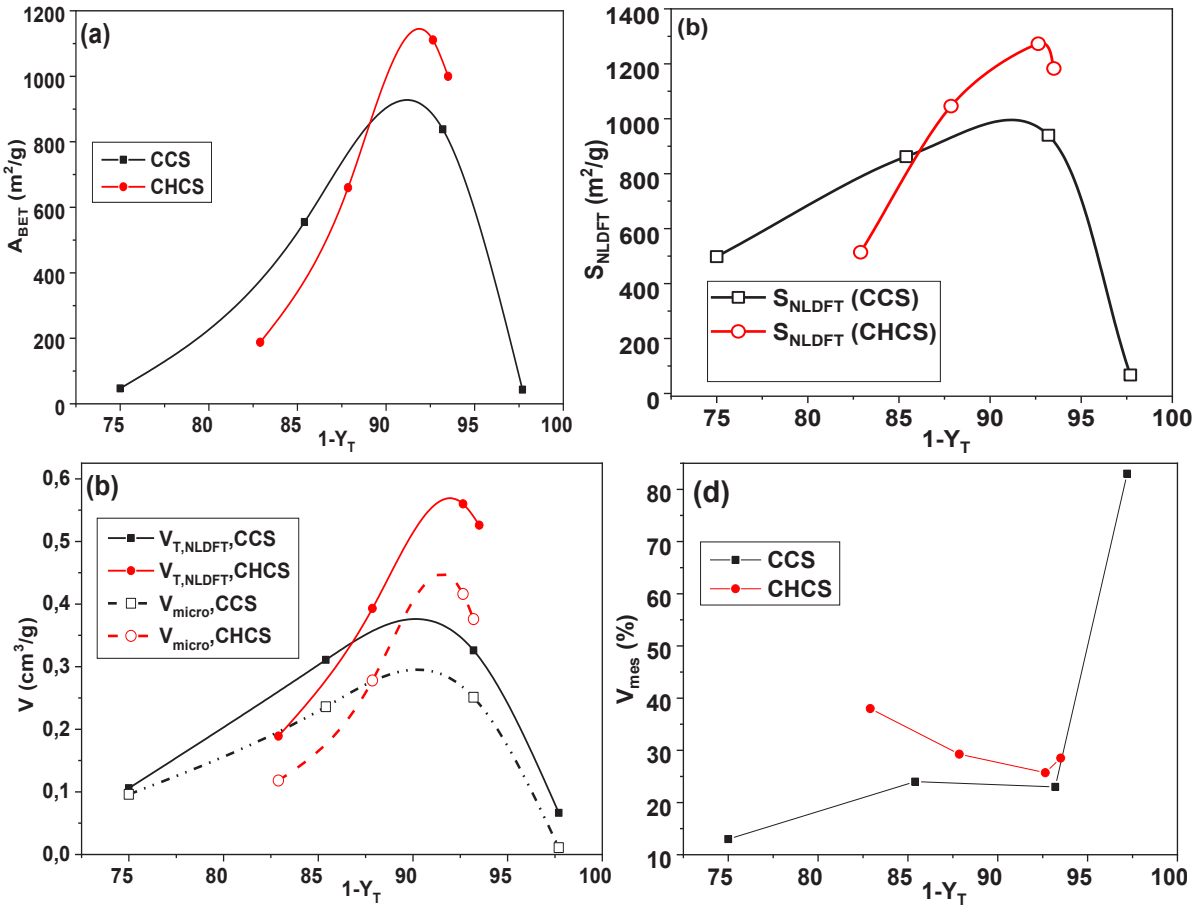

791

792 Figure 3: Surface areas: (a) A_{BET}, and (b) S_{NLDFT}; (c) total volume (full symbols) and
793 micropore volume (empty symbols) and (d) fraction of mesoporosity as a function of $(1 - Y_T)$
794 for CCS and CHCS series. The lines are just guides for the eye.

795

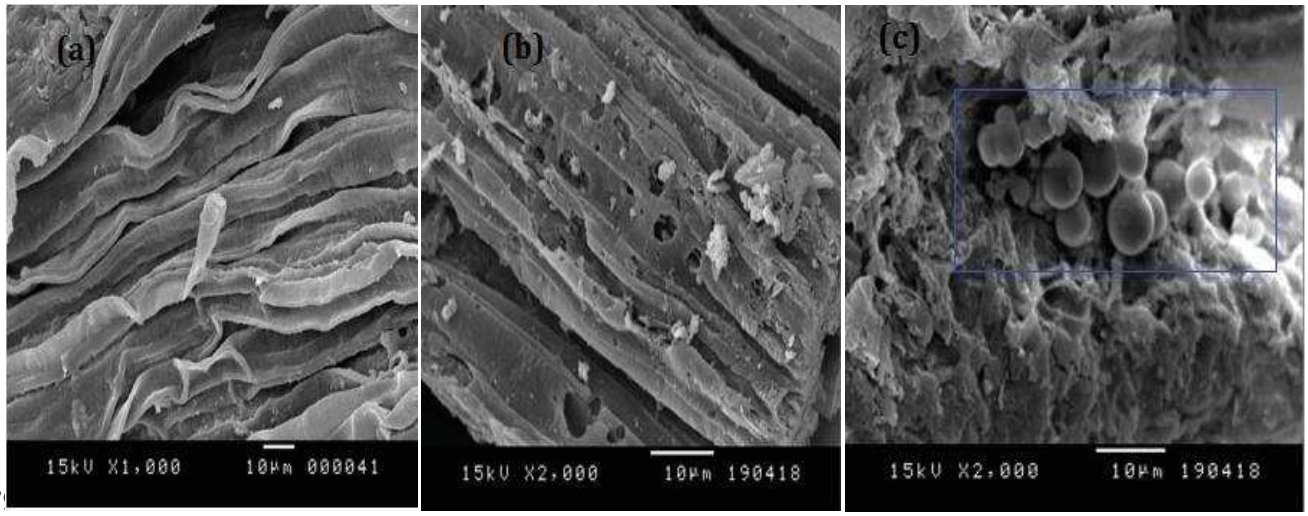

Figure 4: SEM images of: (a) CS; (b) CHCS; and (c) AC2_CHCS.

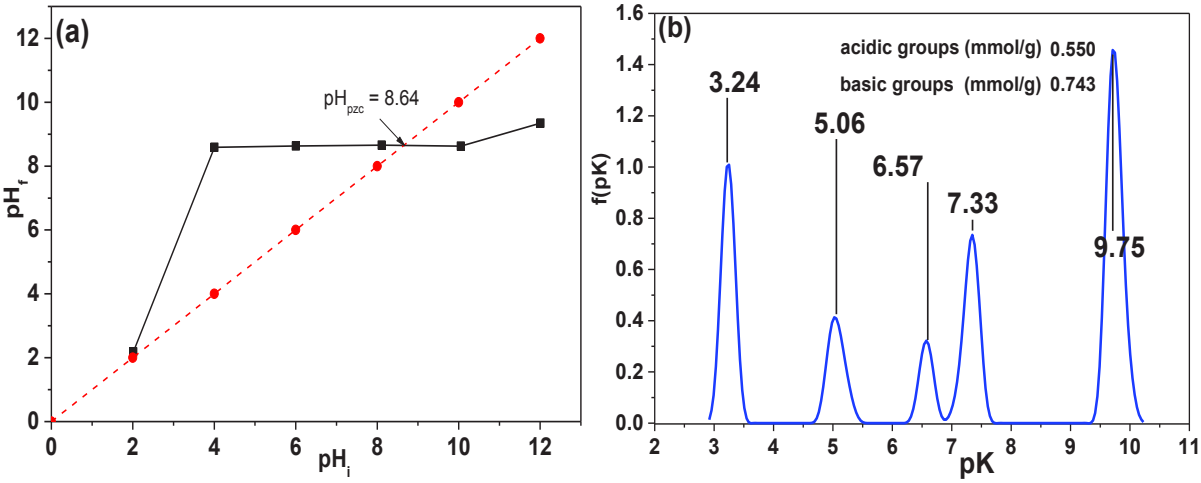

Figure 5: (a) Point of zero charge; and (b) pK_a and amounts of surface groups determined by potentiometric titration of AC2_CHCS.

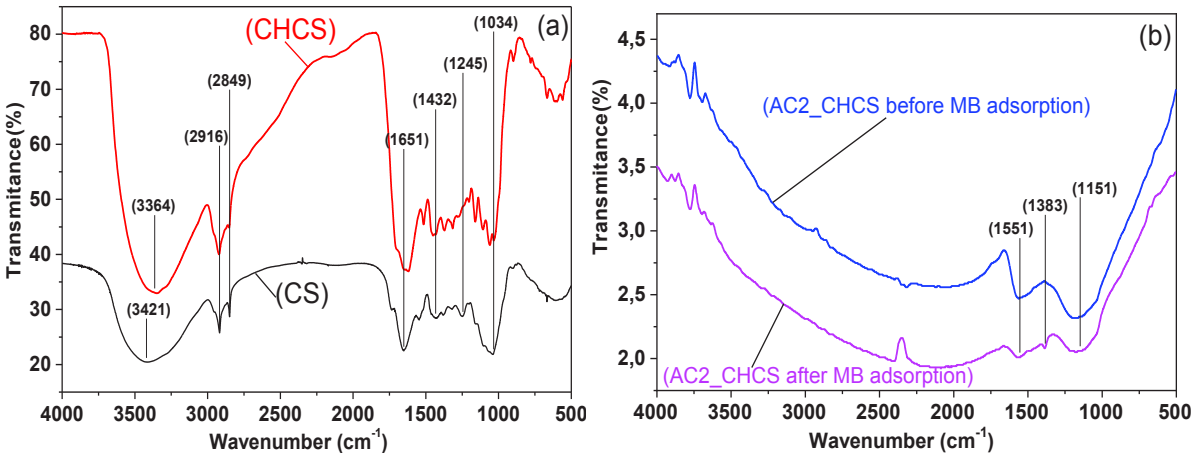

Figure 6: FTIR spectra of: (a) CS and CHCS; and (b) activated carbon (AC2_CHCS) before and after MB adsorption.

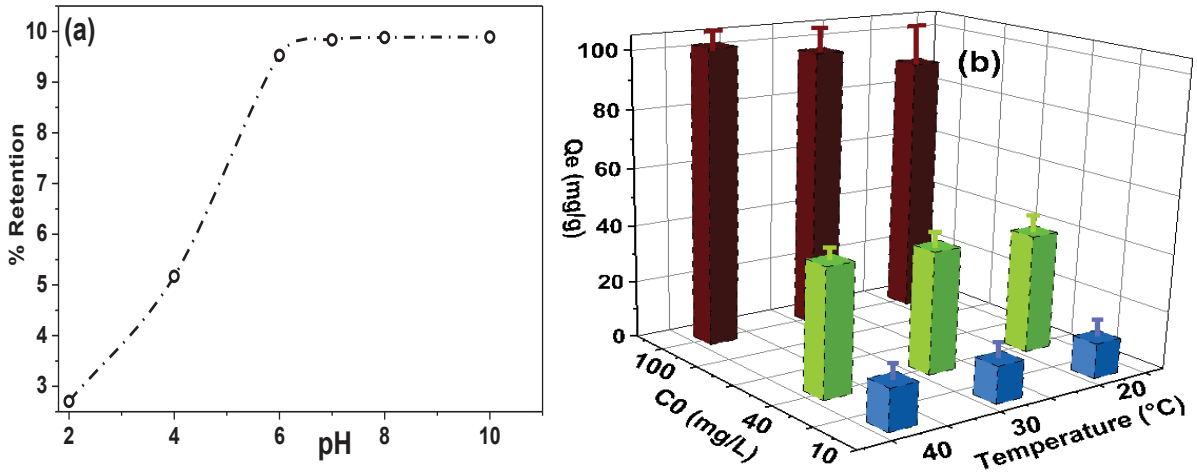

Figure 7: Effect on the MB adsorption capacity of AC2_CHCS of: (a) pH (at 25°C and C_0 = 10 mg/L); and (b) C_0 and temperature (at pH 10). The line in (a) is just a guide for the eye.

819

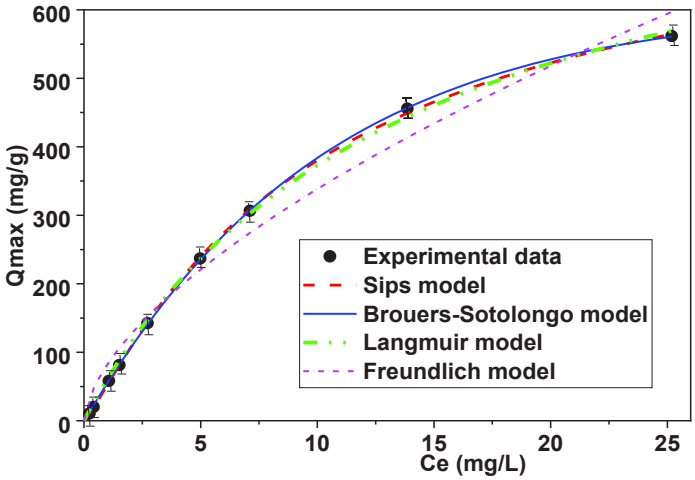

820 Figure 8 : Nonlinear fit of MB isotherm adsorption of AC2_CHCS at pH 10 and 25°C.

821

822